processes

MDPI

Article

Thermal Radiations and Mass Transfer Analysis of the Three-Dimensional Magnetite Carreau Fluid Flow Past a Horizontal Surface of Paraboloid of Revolution

T. Abdeljawad [1,2,3], Asad Ullah [4], Hussam Alrabaiah [5,6], Ikramullah [7], Muhammad Ayaz [8], Waris Khan [9], Ilyas Khan [10,*] and Hidayat Ullah Khan [11]

1 Department of Mathematics and General Sciences, Prince Sultan University, Riyadh 11 586, Saudi Arabia; tabdeljawad@psu.edu.sa
2 Department of Medical Research, China Medical University, Taichung 40402, Taiwan
3 Department of Computer Science and Information Engineering, Asia University, Taichung, Taiwan
4 Institute of Numerical Sciences, Kohat University of Science & Technology, Kohat 26000, Khyber Pakhtunkhwa, Pakistan; asad.ullah@kust.edu.pk
5 College of Engineering, Al Ain University, Al Ain 64141, UAE; hussam89@yahoo.com
6 Department of Mathematics, Tafila Technical University, Tafila 66110, Jordan
7 Department of Physics, Kohat University of Science & Technology, Kohat 26000, Khyber Pakhtunkhwa, Pakistan; ikramullah@kust.edu.pk
8 Department of Mathematics, Abdul Wali Khan University, Mardan 23200, Khyber Pakhtunkhwa, Pakistan; mayazmath@awkum.edu.pk
9 Department of Mathematics, Islamia College University Peshawar, Peshawar 25000, Khyber Pakhtunkhwa, Pakistan; wariskhan758@yahoo.com
10 Faculty of Mathematics and Statistics, Ton Duc Thang University, Ho Chi Minh City 72915, Vietnam
11 Department of Economics, Abbottabad University of Science and Technology (AUST), Abbottabad Havelian 22500, Khyber Pakhtunkhwa, Pakistan; masmaleo@yahoo.com
* Correspondence: ilyaskhan@tdtu.edu.vn

Received: 18 April 2020; Accepted: 22 May 2020; Published: 1 June 2020

Abstract: The dynamics of the 3-dimensional flow of magnetized Carreau fluid past a paraboloid surface of revolution is studied through thermal radiation and mass transfer analysis. The impacts of Brownian motion and chemical reaction rate are considered on the flow dynamics. The system of nonlinear PDEs are converted to coupled ODEs by employing suitable transformation relations. The developed ODEs are solved by applying the standard procedure of homotopy analysis method (HAM). The impacts of various interesting parameters on the state variables of the Carreau fluid (velocity components, temperature, concentration, and shear stress) are explained through various graphs and tables. It is found that the horizontal velocity components augment with the rising magnetic parameter and Grashof number values. The fluid temperature augments with the higher values of the pertinent parameters except Prandtl number. The Nusselet number and fluid concentration enhance with the augmenting Brownian motion parameter. The shear stress augments with the rising Grashof number. The agreement of the obtained and published results validate the accuracy of the employed technique.

Keywords: magnetite–carreau fluid; Brownian motion; mass transfer; thermal radiations; paraboloid of revolution; chemical reaction; magnetic field; homotopy analysis method (HAM)

1. Introduction

Fluids (liquids and gases) are characterized by their ability to flow, as contrasted to solids which possess definite shapes. For decades, the investigators of fluid mechanics have focused on the flow

characteristics of Newtonian and power-law fluids. The main impetus behind this is the fact that in many fluids, the stresses developed during the flow are directly proportional to the local strain. On the other hand, a lot of research groups are working on the generalized Newtonian fluids flow. In such type of fluids, the shear stress depends on the shear rate at a given time. In 1972, Pierre J. Carreau [1,2] presented a model capable of describing the Newtonian fluids (power-law fluids) flow at low (and high) shear rate. A few years later, Bush and Phan-Thien [3] used the Carreau viscosity relation to find the drag force effect of a sphere in a fluid exhibiting shear-thinning as well as elastic properties. Khellaf and Lauriat [4] explained the heat energy transfer flow between two cylinders, in which the inside cylinder was rotatory while the other cylinder was static. The authors employed the Carreau constitutive relation to examine the non-Newtonian shear-thinning model of viscosity. It was concluded that the fluid motion becomes oscillatory with the decreasing flow index or with augmenting Weissenberg number. The motion of the Carreau fluid at an extending wall and at free-stream was analyzed by Khan et al. [5]. In this study, the fluid flow was characterized as shear-thickening $(n > 1)$, Newtonian $(n = 1)$, and shear-thinning $(0 < n < 1)$. The analysis implied that the Carreau fluid shows the Newtonian fluid characteristics at low and power-law fluid characteristics at high shear rates. Olajuwon [6] pointed out that Carreau fluid constitutive equation can describe fluids whose viscosity varies with the increasing deformation rate. The Carreau fluid model gives a finite fluid viscosity in the limit when the shear rate tends to zero in contrast to Ostwald-De Waele or power-law models. Hsu et al. [7] calculated the drag coefficient of a rigid and isolated particle of cylindrical shape flowing in a Carreau fluid. The analysis confirmed that the drag coefficient in this case is smaller due to the Carreau fluid shear-thinning nature as compared to the Newtonian fluid. The study further reveals the direct dependence of the index parameter in the drag coefficient on the relaxation time constant.

It is to be mentioned that the 3-dimensional Carreau fluid flow on complex surfaces like over an upper portion of the aircraft, rocket upper surface, and on car bonnet, etc., has not been undertaken. This may be due to the unavailability of suitable 3D flow solving techniques. The non-Newtonian fluids, for example, structured as well as genetic liquid organisms, human blood, polymeric solutions, and exotic liquids are ubiquitous in this industrialized world. A lot of research has been executed in this direction. The peristaltic flow through a nonsymmetrical channel of a Carreau fluid was explained by Ali and Hayat [8]. The induced magnetic field impact on the transport of Carreau fluid was explained by Hayat et al. [9]. The Carreau fluid motion through an inclined and free surface was analyzed by Tshehla [10]. Elahi et al. [11] discussed the 3D flow of Carreau fluid in a rectangular duct. The investigation of fluid flow in the magnetic field presence to measure its various macroscopic properties is called Magneto Hydro Dynamics (MHD). MHD flow finds its applications in different disciplines like plasma and astrophysics, cooling of nuclear reactors, engineering and technology, and so on. The transfer of heat energy during the MHD fluid flow over a vertical stretching surface was examined by Nazar et al. [12]. He concluded that the rising magnetic field strength results in the reduction of the heat energy loss and coefficient of local skin friction. Ishak et al. [13] discussed the stagnation-point motion in the magnetic field presence towards a stretchable surface. Xu et al. [14] examined analytically the 3D flow of magnetized fluid along with heat energy transfer on a stretchable plate by using a series solution technique. Vajravelu et al. [15] analyzed the convective heat energy transformation over a stretchable surface by applying **B** field. Pop and Na [16] investigated the MHD flow on a stretching and porous surface. Gnaneswara Reddy et al. [17] analyzed the magnetic field and Ohmic heating effects on the viscous nanofluid flow over a nonlinear permeable and extending surface.

The existence of gradients in physical quantities is necessary for the development of various fluxes, which then results in different kinds of flow. The heat energy transfer is mainly associated with the gradients in temperature, this effect is called the Soret effect. The gradients in concentration cause mass transfer flow which gives rise to Dufour effect. These effects play an important role when density differences exist in a system. The phenomena in which heat energy transport takes place, for example, heat energy exchangers, manufacturing of steel, and other cooling processes, the convective heat energy transformation plays a dominant role. The impact due to convective thermal energy transfer flow over

a three-dimensional exponential stretching surface was discussed by Liu et al. [18]. Hayat et al. [19] discussed the Carreau fluid flow of a boundary layer and showed that the rising suction parameter augments (drops) the thickness range (velocity) of the fluid boundary layer. The analysis of thermal energy radiations is of basic importance in solar energy systems, nuclear power reactors, combustion engines and chambers, propulsion engines for high-velocity aircraft, and chemical activities at high operating temperatures. The thermal radiation boundary layer MHD nanofluid flow over an extending surface was examined by Gnaneswara Reddy [20]. Emad [21] examined the effects produced due to the presence of radiation on the electrically conducting fluid motion on an extendable surface. Gnaneswara Reddy [22] investigated the mixed convective magnetized layer slip flow through a permeable surface in the existence of heat energy source and Ohmic effect by taking into account the impacts of radiation energy and chemical reaction. The radiation impact on the convective heat energy transformation in a current carrying fluid over an extendable surface having varying viscosity was investigated by Abo-Eldahab and Elgendy [23]. Gnaneswara Reddy [24] examined the collective impact of Joule heating, thermophoresis and dissipation on a steady magnetized fluid flow on an inclined isothermal surface. The impact of thermal radiations on magnetized fluid motion is numerically investigated in the references [25–27] by taking into account the presence of suction/injection. The mixed convective MHD flow by considering the impacts of joule heating, temperature jump, slip, and viscous dissipation was studied in the references [28,29]. The impact of varying viscosity on a porous plate heated convectively in the presence of thermophoresis effect was considered by Makinde et al. [30]. The study of nanofluid stagnation flow on a stretchable sheet by considering the varying viscosity effect was performed by Khan et al.. Ibrahim and Makinde [31] further expanded their previous work to examine the convective boundary value flow of Casson fluid. The mass and heat energy transformation properties of Newtonian as well as non-Newtonian fluids by considering the thermal radiation impact are discussed in the references [32–34]. The impact of chemical reaction and thermal radiations on the MHD flow was considered by Hayat et al. [35]. Shehzad et al. [36] numerically examined the 3D Casson fluid motion within a permeable medium by considering the effect of internal heat energy. The impacts of radiation and chemically reactive components on a magnetized convection flow near a vertical moving wall was examined by Gnaneswara Reddy [37]. The mass and heat energy transformation properties of Newtonian as well as non-Newtonian fluids were investigated by Raju et al. [38,39] in the existence of thermal radiation.

Motivated by the above studies, we want to analytically examine the 3D Carreau fluid MHD flow over a horizontal paraboloid surface of revolution through thermal radiation and mass transfer analysis by considering the chemical reaction and Brownian motion effects. The geometry and mathematical modeling of the problem is given in Section 2. The solution methodology used is explained in Section 3. The impacts of pertinent parameters on the various aspects of the Carreau fluid flow are explained through graphs in Section 4. The comparison and calculations of Sherwood and Nuselt numbers as well as the shear stresses are explained through different tables in Section 5. The work is concluded in Section 6.

2. Formulation of the Problem

We analyze the $3D$ nonlinear and magnetized mixed convective Carreau fluid flow. The geometry of the problem is selected such that the $x-$axis lies parallel to the surface. The **B**-field is applied normal to the sheet, i.e., along the $z-$axis as shown Figure 1. The basic relation that governs the Carreau fluid flow is [40,41]

$$\tau = \left[\eta_\infty + (\eta_0 - \eta_\infty)\left(1 + (\lambda\dot{\gamma})^2\right)^{\frac{n-1}{2}}\right]\dot{\gamma}, \tag{1}$$

where τ denotes the extra stress tensor, η_∞ (η_0) is the infinity shear rate (zero shear rate) viscosity, λ is the time constant, n is the index of power-law, and $\dot{\gamma}$ is given by [4]

$$\dot{\gamma} = \sqrt{\frac{1}{2}\sum_i\sum_j \dot{\gamma}_{ij}\dot{\gamma}_{ji}} = \sqrt{\frac{1}{2}\prod}, \tag{2}$$

where $\prod$ is the second invariant of the strain-rate tensor. Assuming $\eta_\infty = 0$, we have from Equation (1),

$$\tau = \left[\eta_0\left(1 + (\lambda\dot{\gamma})^2\right)^{\frac{n-1}{2}}\right]\dot{\gamma}. \tag{3}$$

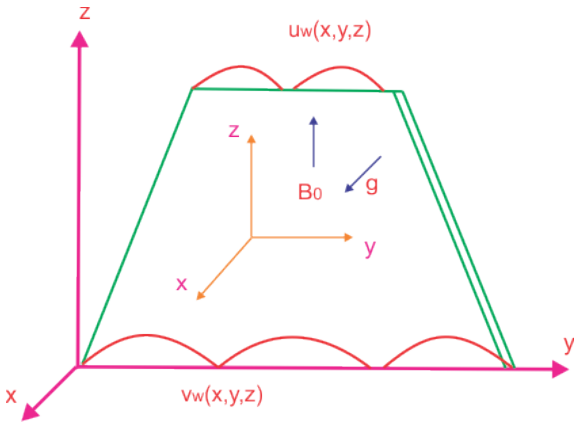

Figure 1. Geoemtrical demonstrarion of the physical problem.

We assume that $u_w = U_0(b + x + y)^p$, $v_w = 0$, $Z = d(l + x + y)^{\frac{1-p}{2}}$, $p \neq 1$, where d, l and b are constants. The model equations that govern the dynamics of the magnetized Carreua fluid are

$$\frac{\partial u}{\partial x} + \frac{\partial v}{\partial y} + \frac{\partial w}{\partial z} = 0, \tag{4}$$

$$u\frac{\partial u}{\partial x} + v\frac{\partial u}{\partial y} + w\frac{\partial u}{\partial z} = \nu\frac{\partial^2 u}{\partial z^2}\left[1 + \Gamma^2\left(\frac{\partial u}{\partial z}\right)^2\right]^{\frac{n-1}{2}} + \nu(n-1)\Gamma^2\frac{\partial^2 u}{\partial z^2}\left(\frac{\partial u}{\partial z}\right)^2\left[1 + \Gamma^2\left(\frac{\partial u}{\partial z}\right)^2\right]^{\frac{n-3}{2}} + g\beta\left(\frac{m+1}{2}\right)(T - T_\infty) - \frac{\sigma B_0^2 u}{\rho}, \tag{5}$$

$$u\frac{\partial v}{\partial x} + v\frac{\partial v}{\partial y} + w\frac{\partial v}{\partial z} = \nu\frac{\partial^2 v}{\partial z^2}\left[1 + \Gamma^2\left(\frac{\partial v}{\partial z}\right)^2\right]^{\frac{n-1}{2}} + \nu(n-1)\Gamma^2\frac{\partial^2 v}{\partial z^2}\left(\frac{\partial v}{\partial z}\right)^2\left[1 + \Gamma^2\left(\frac{\partial v}{\partial z}\right)^2\right]^{\frac{n-3}{2}} + g\beta\left(\frac{m+1}{2}\right)(T - T_\infty) - \frac{\sigma B_0^2 v}{\rho}, \tag{6}$$

$$(\rho C_p)\left[u\frac{\partial T}{\partial x} + v\frac{\partial T}{\partial y} + w\frac{\partial T}{\partial z}\right] = \kappa\frac{\partial^2 T}{\partial z^2} + Q_0(T_w - T_\infty)exp\left[-qz\sqrt{\frac{m+1}{2}\frac{U_0}{\nu}}(x + y + b)^{\frac{m-1}{2}}\right] + q''' - \frac{\partial q_r}{\partial z}, \tag{7}$$

$$u\frac{\partial C}{\partial x} + v\frac{\partial C}{\partial y} + w\frac{\partial C}{\partial z} = D_m\frac{\partial^2 C}{\partial z^2} + \frac{D_T}{T_\infty}\frac{\partial^2 T}{\partial z^2} - \hat{k}(C - C_\infty). \tag{8}$$

The boundary restrictions on the system are given by

$$\begin{aligned} u = U_w,\ v = V_w,\ w = 0,\ T = T_w,\ C = C_w,\ \text{at}\ z = A(b + x + y)^{\frac{1-m}{2}}, \\ u \to 0,\ v \to 0,\ T \to T_\infty,\ C \to C_\infty\ \text{at}\ z \to \infty. \end{aligned} \tag{9}$$

Here, u, v and w are the velocity Cartesian components, Γ is the time constant, ν (k) is the kinematic fluid viscosity (thermal conductivity), $\hat{k}$ is the dimensional parameter of the chemical reaction, D_m is the mass diffusivity, C (C_∞) is the fluid concentration (ambient fluid concentration), and C_p is the heat capacity. The nonuniform heat source (q''') is given by [42]

$$q''' = \frac{kU_0}{\nu(b+x+y)^{1-m}}\Big[(T_w - T_\infty)\tilde{A}f' + (T - T_\infty)\tilde{B}\Big], \tag{10}$$

where $\tilde{A} > 0$ and $\tilde{B} > 0$ show the reflection, whereas $-\tilde{A} > 0$ and $-\tilde{B} > 0$ show the heat absorption inside the system. The radiation flux q_r is defined as [6,42]

$$q_r = -\frac{4\sigma^s}{3k_1}\frac{\partial T^4}{\partial y}, \tag{11}$$

where σ^s is the Stefan–Boltzmann constant and k_1 is the average absorption coefficient. Taylor expanding T^4 about the fixed temperature T_∞ and ignoring T_∞^4 and higher order terms in Equation (11), we get

$$\frac{\partial q_r}{\partial z} = -\frac{16\sigma^s T_\infty^3}{3k_1}\frac{\partial^2 T}{\partial z^2}. \tag{12}$$

Assume the following transformations [42,43]:

$$\psi(x,y,z) = \sqrt{\frac{2\nu U_0}{m+1}}(b+x+y)^{\frac{m+1}{2}} f(\eta),\ \ \xi(x,y,z) = \sqrt{\frac{2\nu U_0}{m+1}}(b+x+y)^{\frac{m+1}{2}} g(\eta), \tag{13}$$

$$u = \frac{\partial u}{\partial z},\ \ v = \frac{\partial \xi}{\partial z},\ \ w = \left(\frac{\partial^2 \psi}{\partial z \partial y} + \frac{\partial^2 \xi}{\partial z \partial x}\right)\ \ \eta = z(b+x+y)^{\frac{m-1}{2}}\sqrt{\frac{(m+1)U_0}{2\nu}}, \tag{14}$$

$$T_w(x,y) = A(b+x+y)^{\frac{1-m}{2}},\ C_w(x,y) = A(b+x+y)^{\frac{1-m}{2}},\ \theta(\eta) = \frac{T - T_\infty}{T_w - T_\infty},\ \phi(\eta) = \frac{C - C_\infty}{C_w - C_\infty}. \tag{15}$$

From Equations (13)–(15), we have

$$\begin{aligned} u = U_0 f'(b+x+y)^m,\ v = U_0 g'(b+x+y)^m, \\ w = -\sqrt{\frac{2\nu U_0}{m+1}}(b+x+y)^{\frac{m-1}{2}}\Big[(f(\eta)+g(\eta))\Big(\frac{1-m}{2}\Big) + \eta(f(\eta)' + g(\eta)')\Big(\frac{m-1}{2}\Big)\Big]. \end{aligned} \tag{16}$$

Using Equations (10) and (12) together with Equations (17) and (18) in Equations (4)–(8), we get

$$\Big[1 + nWe^2(f'')^2\Big]\Big[1 + We^2(f'')^2\Big]^{\frac{n-3}{2}} f''' - \Big(\frac{m-1}{m+1}\Big)(f+g)f'' + Gr\theta - Mf' = 0, \tag{17}$$

$$\Big[1 + nWe^2(g'')^2\Big]\Big[1 + We^2(g'')^2\Big]^{\frac{n-3}{2}} g''' - \Big(\frac{m-1}{m+1}\Big)(f+g)g'' + Gr\theta - Mg' = 0, \tag{18}$$

$$\Big(1 + Rd\Big)\theta'' - Pr\Big(\frac{m-1}{m+1}\Big)(f+g)\theta' + \frac{2}{m+1}\Big[Pr\gamma e^{-q\eta} + \tilde{A}f' + \tilde{B}\theta\Big] = 0, \tag{19}$$

$$\phi'' - Sc\Big(\frac{m-1}{m+1}\Big)(f+g)\phi' + \frac{Nt}{Nb}\theta'' + \frac{2\hat{k}}{m+1}Sc\phi = 0, \tag{20}$$

where Equation (4) is satisfied identically.

Here, $Pr = \frac{\nu\rho C_p}{k}$ denotes the Prandtl number, $We = \sqrt{\frac{\Gamma^2(m+1)U_0^3(b+x+y)^{3m-1}}{2\nu}}$ is the Weissenberg number, $Gr = \frac{g\beta(T_w - T\infty)(b+x+y)^{1-2m}}{U_0^2}$ is the Grashof number, $\gamma = \frac{Q_0(b+x+y)^{1-m}}{(\rho C_p)U_0}$ demonstrates the internal heat source, $Sc = \frac{\nu}{Dm}$ is the Schmidt number, $\hat{k}$ is the parameter of chemical reaction, $Nt = \frac{\tau D_T T_0}{kT_\infty}$ is the thermoporesis parameter, $Nb = \frac{\tau D_w C_0}{kC_\infty}$ is the Brownian motion parameter, and $Rd = \frac{16\sigma^* T_\infty^3}{3kk_e}$ is the radiation parameter. The boundary restrictions of the system are nondimensional, as discussed in the references [44,45]. The boundary restrictions on the system must be set at $z = 0$ because the exceeding of the z_{min}, but it is impossible in practice that all the restrictions be set at $z = 0$ at the

parabolic upper horizontal surface. As a result, it is impossible to use $z = 0$ in the similarity variables. Choosing $z = (b + x + y)^{\frac{1-m}{2}}$ at the slot starting point gives the minimum value of the similarity variable η and is given by

$$\Lambda = A\sqrt{\frac{(m+1)U_0}{2\nu}} = \eta. \tag{21}$$

Using Equations (13) and (15) in Equation (9), we get

$$\begin{gathered}\frac{df}{d\Lambda} = 1, f(\Lambda) = \Lambda\Big(\frac{1-m}{1+m}\Big)f(\Lambda)', \frac{dg}{d\Lambda} = c, g(\Lambda) = \Lambda\Big(\frac{1-m}{1+m}\Big)g(\Lambda)', \theta(\Lambda) = 1, \phi(\Lambda) = 1 \text{ at } \Lambda = 0, \\ \frac{df}{d\Lambda} \to 0, \frac{dg}{d\Lambda} \to 0, \frac{d\theta}{d\Lambda} \to 0, \frac{d\phi}{d\Lambda} \to 0, \text{ at } \Lambda = \infty.\end{gathered} \tag{22}$$

It is to be noted here that the boundary restrictions in Equation (22) depend on Λ, while Equations (17)–(20) depend on the independent variable η. For this, the domain $[\Lambda, \infty]$ is transformed to $[0, \infty]$ as discussed by Abegunrin [45]. Therefore, assume that $\varsigma = -(\Lambda - \eta)$, then $F(\eta - \Lambda) = F(\varsigma) = f(\eta)$, $G(\eta - \Lambda) = G(\varsigma) = g(\eta)$, $\Theta(\eta - \Lambda) = \Theta(\varsigma) = \Theta(\eta)$, and $\Phi(\eta - \Lambda) = \Phi(\varsigma) = \Phi(\eta)$. From these assumptions, Equations (17)–(20) and Equation (22) are given by

$$\Big[1 + nWe^2(F'')^2\Big]\Big[1 + We^2(F'')^2\Big]^{\frac{n-3}{2}}F''' - \Big(\frac{m-1}{m+1}\Big)(F+G)F'' + Gr\Theta - MF' = 0, \tag{23}$$

$$\Big[1 + nWe^2(G'')^2\Big]\Big[1 + We^2(G'')^2\Big]^{\frac{n-3}{2}}G''' - \Big(\frac{m-1}{m+1}\Big)(F+G)G'' + Gr\Theta - MG' = 0, \tag{24}$$

$$\Big(1 + Rd\Big)\Theta'' - Pr\Big(\frac{m-1}{m+1}\Big)(F+G)\Theta' + \frac{2}{m+1}\Big[Pr\gamma e^{-q\varsigma} + \tilde{A}F' + \tilde{B}\Theta\Big] = 0, \tag{25}$$

$$\Phi'' - Sc\Big(\frac{m-1}{m+1}\Big)(F+G)\Phi' + \frac{Nt}{Nb}\Theta'' + \frac{2\hat{k}}{m+1}Sc\Phi = 0, \tag{26}$$

$$\begin{gathered}\frac{dF}{d\varsigma} = 1, F(\varsigma) = \Lambda\Big(\frac{1-m}{1+m}\Big)F(\varsigma)', \frac{dG}{d\varsigma} = c, G(\varsigma) = \Lambda\Big(\frac{1-m}{1+m}\Big)G(\varsigma)', \Theta(\varsigma) = 1, \Phi(\varsigma) = 1 \text{ at } \varsigma = 0, \\ \frac{dF}{d\varsigma} \to 0, \frac{dG}{d\varsigma} \to 0, \frac{d\Theta}{d\varsigma} \to 0, \frac{d\Phi}{d\varsigma} \to 0, \text{ at } \varsigma = \infty.\end{gathered} \tag{27}$$

The engineering quantities of interest are given by

$$\begin{gathered}C_{fx} = \frac{\tau_{wx}U_w^2}{\rho\sqrt{\frac{m+1}{2}}}, \quad C_{fy} = \frac{\tau_{wy}v_w^2}{\rho\sqrt{\frac{m+1}{2}}}, \\ Nu_{x,y} = \frac{(b+x+y)q_w}{k(T_w - T_\infty)\sqrt{\frac{m+1}{2}}}, \quad Sh_x = \frac{(b+x+y)\frac{\partial C}{\partial z}}{(C_w - C_\infty)\sqrt{\frac{m+1}{2}}},\end{gathered} \tag{28}$$

where,

$$\begin{gathered}\tau_{wx} = \Big(\mu\frac{\partial u}{\partial z}\Big[1 + \Gamma^2\Big(\frac{\partial u}{\partial z}\Big)^2\Big]\Big)_{z=U_0(b+x+y)^{\frac{1-m}{2}}}, \quad \tau_{wy} = \Big(\mu\frac{\partial v}{\partial z}\Big[1 + \Gamma^2\Big(\frac{\partial v}{\partial z}\Big)^2\Big]\Big)_{z=U_0(b+x+y)^{\frac{1-m}{2}}}, \\ q_{xy} = \Big(-k\frac{\partial T}{\partial z}\Big)_{z=U_0(b+x+y)^{\frac{1-m}{2}}}.\end{gathered} \tag{29}$$

From above, we can write

$$\begin{gathered}C_{fx}(Re^{1/2}) = F''(0)\Big[1 + We(F''(0)^2\Big]^{\frac{n-1}{2}}, \quad C_{fy}(Re^{1/2}) = G''(0)\Big[1 + We(G''(0)^2\Big]^{\frac{n-1}{2}}, \\ Nu_{xy}(Re)^{-1/2} = -\Theta'(0), \quad Sh_x(Re)^{-1/2} = -\sqrt{\frac{m+1}{2}}\phi'(0).\end{gathered} \tag{30}$$

3. Analytical Solution

The basic mechanism of HAM is explained by Liao in his PhD thesis [46]. The advantages and comparison of HAM are discussed in reference [47]. Liao used a topological concept known as "Homotopy". He used two different continuous functions $\zeta_1(\hat{x})$ and $\zeta_2(\hat{x})$ defined over the two spaces $\hat{X}$ and $\hat{Y}$. The basic theory of the transformation is based on linking the closed unit interval with the topological spaces defined, as given below:

$$\tilde{\Psi} : \hat{X} \times [0,1] \rightarrow \hat{Y}, \tag{31}$$

where $\tilde{\Psi}[\hat{x},0] = \zeta_1(\hat{x})$ and $\tilde{\Psi}[\hat{x},1] = \zeta_2(\hat{x})$ holds $\forall \hat{x} \in \hat{X}$. The transformation given in Equation (31) is called homotopic transformation. The set of Equations (23)–(26), together with the boundary restrictions (27) are solved with HAM [48], by choosing suitable initial guesses F_0, G_0, Θ_0, and Φ_0 with the corresponding liner operators defined as

$$L_{\bar{F}}(\bar{F}) = \bar{F}''', \; L_{\bar{G}}(\bar{G}) = \bar{G}''' \; L_{\bar{\Theta}}(\bar{\Theta}) = \bar{\Theta}'', \text{ and } L_{\bar{\Phi}}(\bar{\Phi}) = \bar{\Phi}'', \tag{32}$$

that satisfies

$$L_{\bar{F}}(c_1 + c_2\varsigma + c_3\varsigma^2) = 0, \; L_{\bar{G}}(c_4 + c_5\varsigma + c_6\varsigma^2) = 0, \; L_{\bar{\Theta}}(c_7 + c_8\varsigma) = 0, \text{and} L_{\bar{\Phi}}(c_9 + c_{10}\varsigma) = 0. \tag{33}$$

4. Results and Discussion

Here, we explain graphically the impacts due to the varying values of the associated parameters in the state variables (velocity, shear stress, temperature, and concentration). We also explain the variation of Sherwood and Nusselet numbers as well as the skin friction, respectively. Figures 2–17 show the variation in the state variables, whereas Figures 18–20 represent the variation in the Sherwood number, Nusselt number, and the skin friction with the changing associated parameters values.

We plotted the impact of the changing magnetic parameter (M) values over $F^{'}(\zeta)$ and $G^{'}(\zeta)$ (horizontal velocity profiles), respectively, in Figure 2a,b. It is found that at a given M, both velocity components vary inversely with higher values of ζ almost at the same manner. It is clear that the increasing M drops the profiles of both these components. The drop in the profiles is prominent at the smaller values of ζ. The increasing magnetic field produces higher Lorentz force which results in the reduction of velocities.

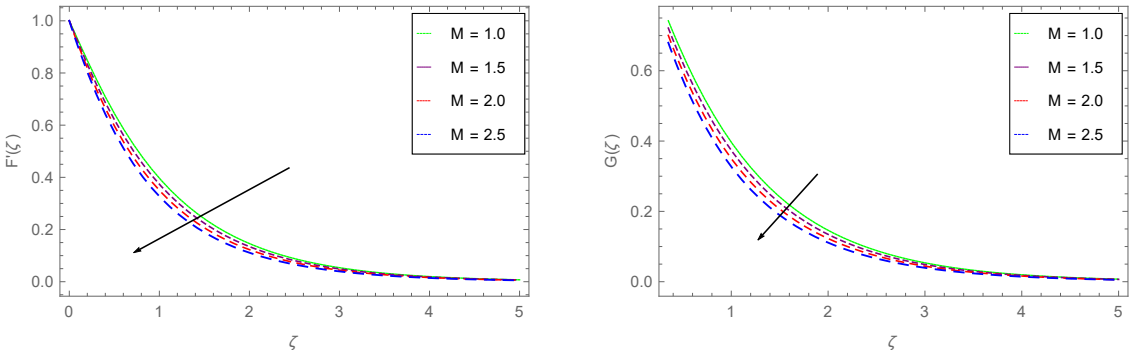

(**a**) (**b**)

Figure 2. Impact of M on (**a**) $F^{'}(\zeta)$ and (**b**) $G^{'}(\zeta)$.

The dependence of the vertical components of velocity ($F(\zeta)$ and $G(\zeta)$) on the stretching rate ratio (c) is plotted in Figure 3a,b. It is clear that the component $F(\zeta)$ drops while the other component $G(\zeta)$ rises with the increasing c values. The drop in $F(\zeta)$ is very minute and is visible beyond $\zeta = 1.2$.

The rising behavior of $G(\zeta)$ with the higher stretching rate ratio is more prominent, as can be seen in Figure 3b.

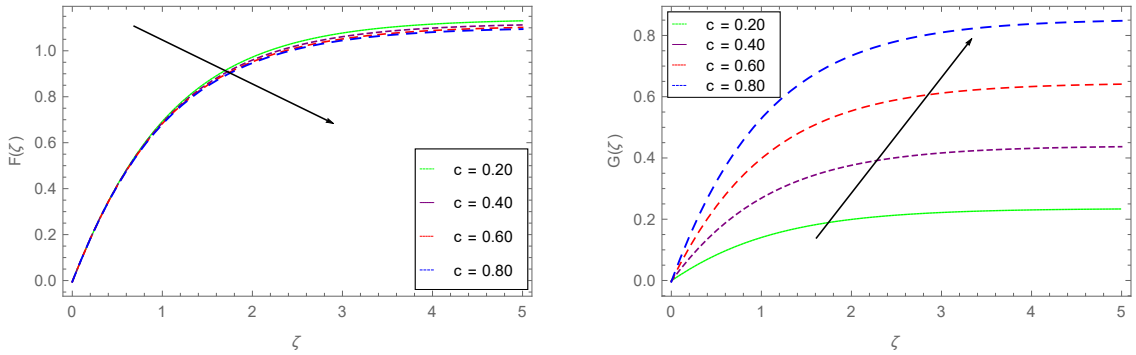

(**a**) (**b**)

Figure 3. (**a**) Impact of c on $F(\zeta)$ and (**b**) $G(\zeta)$.

The dependence of $F^{'}(\zeta)$ and $G^{'}(\zeta)$ on the stretching rate ratio c is depicted in Figure 4a,b. We observe that the component $F^{'}(\zeta)$ drops while the other horizontal component $G^{'}(\zeta)$ rises with the augmenting c values. These dropping and enhancing behaviors are more obvious for the smaller values of ζ, i.e., close to the wall.

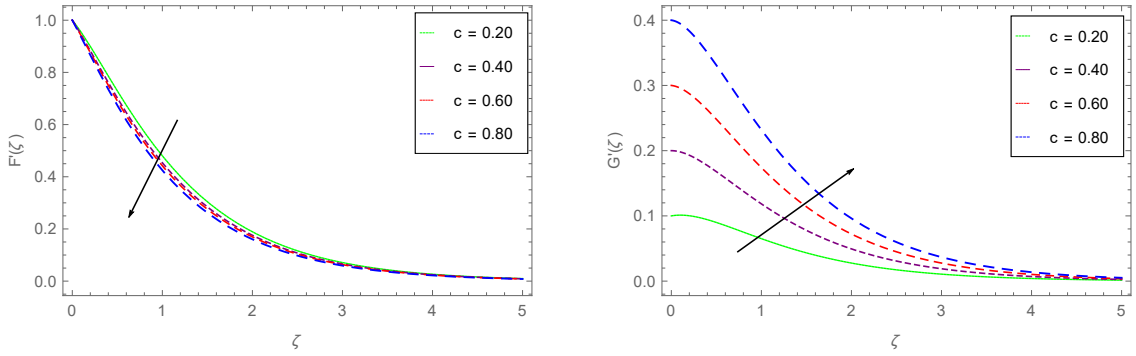

(**a**) (**b**)

Figure 4. (**a**) Impact of c on $F^{'}(\zeta)$ and (**b**) $G^{'}(\zeta)$.

The variation of the shear stress profiles $F^{''}(\zeta)$ and $G^{''}(\zeta)$ with the varying values of stretching rate ratio is explained in Figure 5a,b. We see from Figure 5a that up to about $\zeta = 1.0$, the shear stress $F^{''}(\zeta)$ drops; while beyond it rises with larger c values. The shear stress $G^{''}(\zeta)$ drops with higher values of c, as is clear from Figure 5b. The rate at which $G^{''}(\zeta)$ drops is larger for smaller values of ζ. As c is the ratio between two stretching velocities, if one component enhances, then the other must drop with higher c values, as observed in all cases in which c is changing.

The influence of We (Weissenberg number) on the horizontal components of velocity is sketched respectively in Figure 6a,b. It is seen from Figure 6a that the component $F^{'}(\zeta)$ augments with the increasing Weissenberg number values. This increase in $F^{'}(\zeta)$ with We is dominant up to $\zeta = 03$. The rate at which $F^{'}(\zeta)$ enhances is larger for higher We. A decreasing trend is observed for the horizontal component $G^{'}(\zeta)$ with increasing We, as can be seen from Figure 6b. Here, the rate at which $G^{'}(\zeta)$ drops is larger for smaller We values.

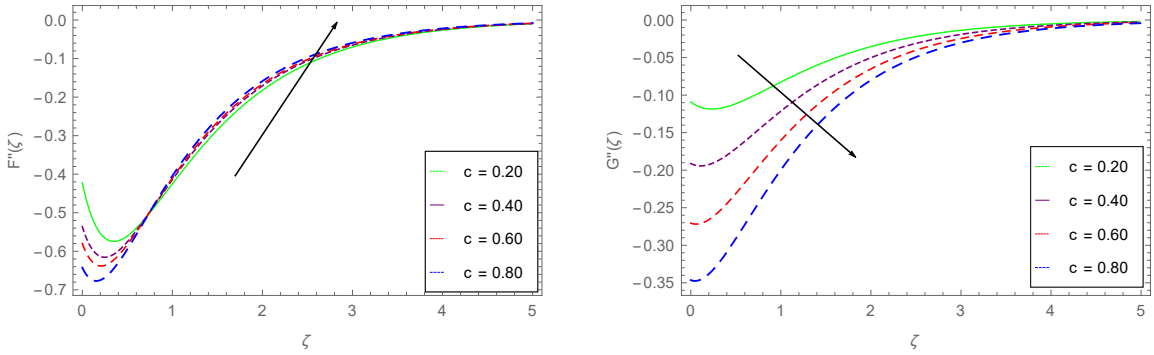

(**a**) (**b**)

Figure 5. Impact of c on the shear stresses (**a**) $F^{''}(\zeta)$ and (**b**) $G^{''}(\zeta)$.

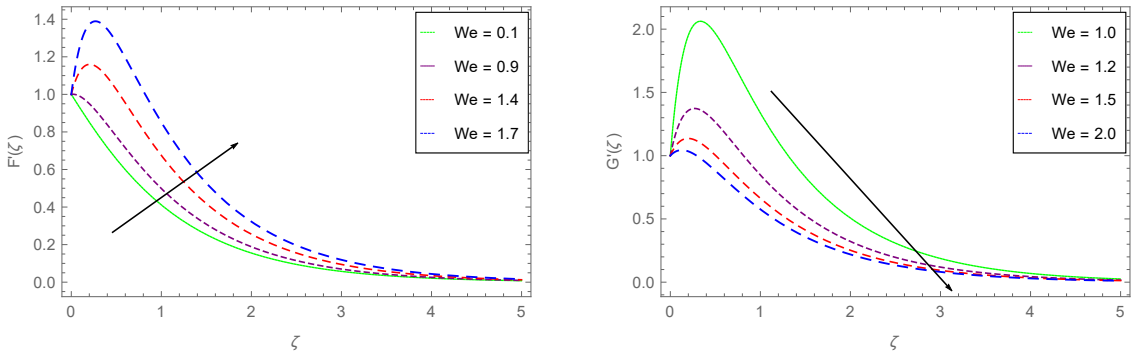

(**a**) (**b**)

Figure 6. Impact of We on the horizontal velocity components (**a**) $F^{'}(\zeta)$ and (**b**) $G^{'}(\zeta)$.

The influence of Λ upon $F(\zeta)$ and $G(\zeta)$ (the vertical velocity profiles) is portrayed in Figure 7. We observe that both the vertical components show almost similar increasing dependence with the augmenting values of Λ.

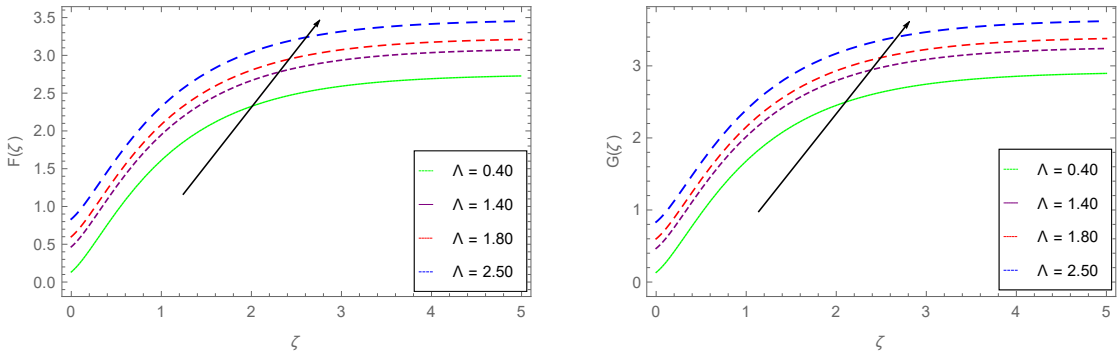

(**a**) (**b**)

Figure 7. Impact of Λ on (**a**) $F(\zeta)$ and (**b**) $G(\zeta)$.

The influence of Λ upon $F^{'}(\zeta)$ and $G^{'}(\zeta)$ profiles is portrayed in Figure 8. We observe that both these velocity components show decreasing behavior with the augmenting Λ values. The spacing among the $G^{'}(\zeta)$ curves is larger for higher Λ values as compared to the spacing between $F^{'}(\zeta)$ curves.

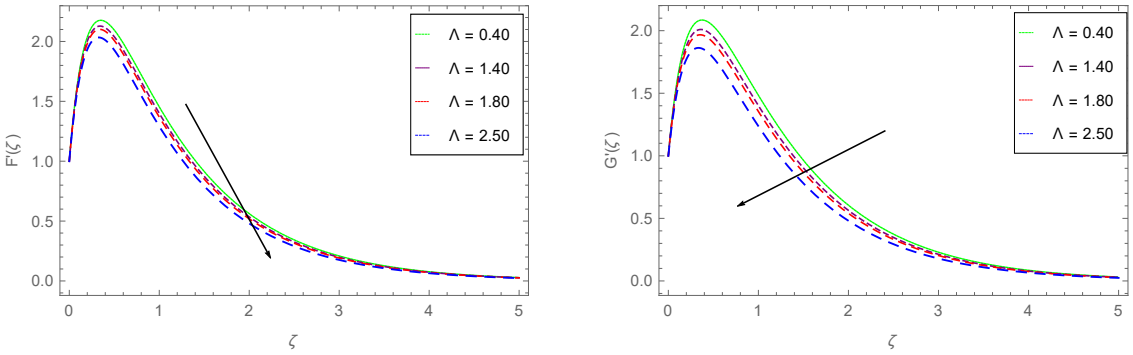

Figure 8. Impact of Λ on (**a**) $F^{'}(\zeta)$ and (**b**) $G^{'}(\zeta)$.

The dependence of the shear stress profiles $F^{''}(\zeta)$ and $G^{''}(\zeta)$ on Λ is portrayed in Figure 9. It is obvious from the figures that both the shear stress components show almost the same rising behavior. Initially, up to about $\zeta = 0.5$, the shear stress profiles drop with higher Λ, while up to $\zeta = 4.0$, both these shear stress components augment with higher rate. Beyond $\zeta = 4.0$, the profiles remain almost constant.

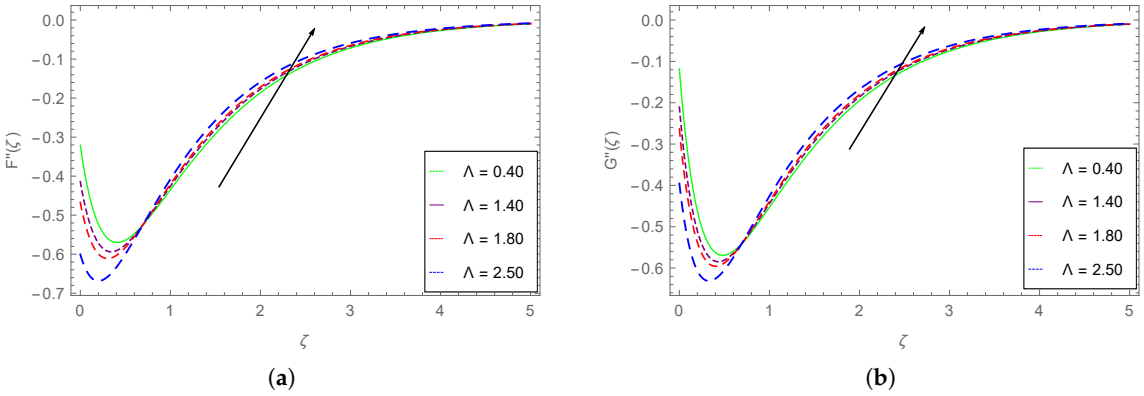

Figure 9. Impact of Λ on the shear stress profiles (**a**) $F^{''}(\zeta)$ and (**b**) $G^{''}(\zeta)$.

The impact of the Grashof number Gr $(1.0, 3.0, 5.0, 7.0)$ on $F(\zeta)$ and $G(\zeta)$ profiles is plotted in Figure 10. These graphs show that the velocity components display a similar rising trend with the larger values of the Grashof number. The spacing between the curves for augmenting Gr values is almost constant. This physically means that lager buoyancy forces (associated with higher Gr values) augment the velocity components of the magnetic Carreau fluid.

The impact of the varying values of Grashof number Gr on the horizontal velocity profiles are depicted in Figure 11. These graphs show that the velocity components follow similar increasing tendency with the augmenting Grashof number. The augmenting trend in these components is more obvious for the intermediate values of ζ. This again means that the larger buoyancy forces (high Gr values) augment the Carreau fluid velocity components.

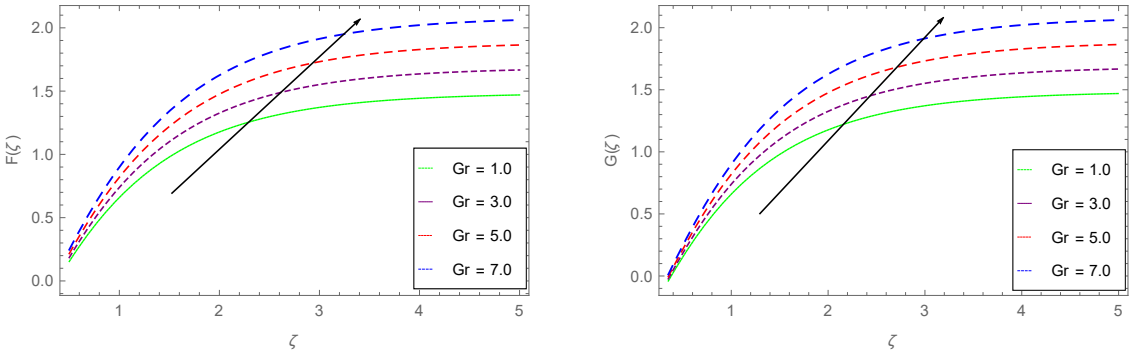

Figure 10. Impact of Gr on (**a**) $F(\zeta)$ and (**b**) $G(\zeta)$.

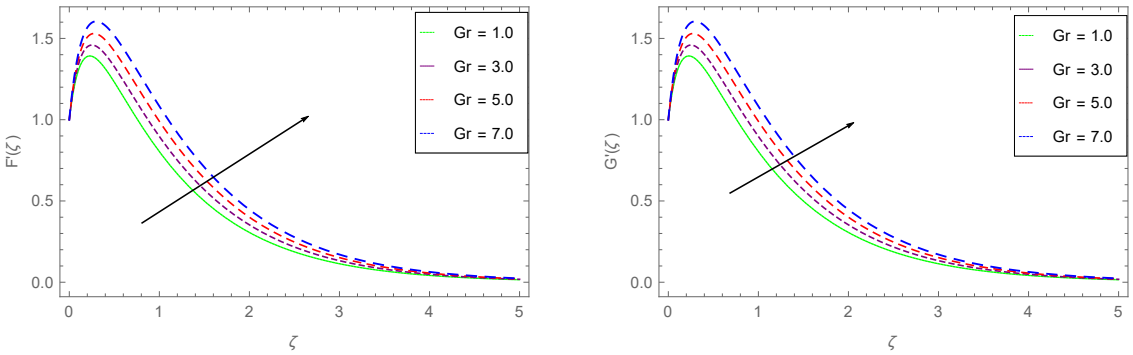

Figure 11. Impact of Gr on (**a**) $F^{'}(\zeta)$ and (**b**) $G^{'}(\zeta)$.

The variation of the shear stress components $F^{''}(\zeta)$ and $G^{''}(\zeta)$ with varying values of Gr is shown in Figure 12. Both these components show a decreasing trend with higher Gr. The decreasing tendency is more obvious for smaller values of ζ. The spacing between different $F^{''}(\zeta)$ curves is larger compared to spacing between $G^{''}(\zeta)$ curves for varying Gr values. Thus, the increasing buoyancy forces with the higher values of Gr result in depreciating the shear stresses.

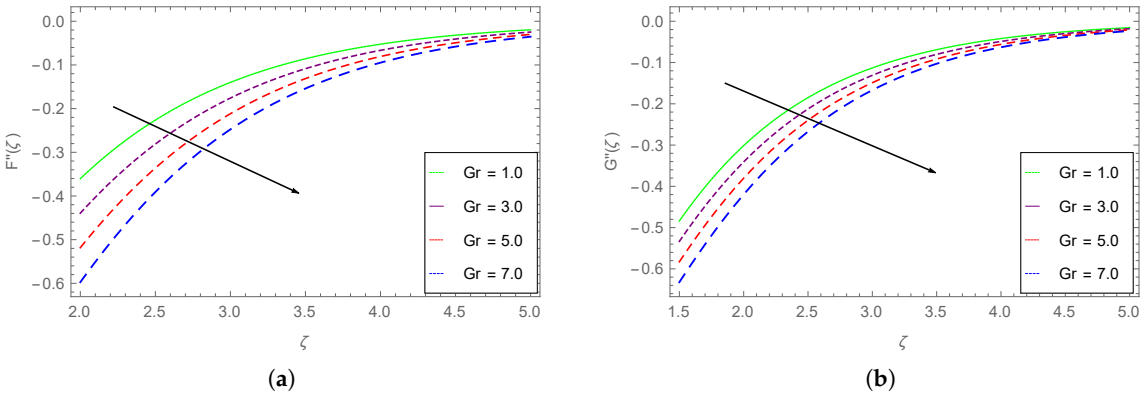

Figure 12. Impact of Gr on (**a**) $F^{''}(\zeta)$ and (**b**) $G^{''}(\zeta)$.

The temperature distributions of the magnetized Carreau fluid with the changing Prandtl number (Pr) and radiation parameter (Rd) are plotted in Figure 13a,b, respectively. From Figure 13a, we see that at a given value of Pr, the Carreau fluid temperature reduces with the larger ζ. The rate at which

temperature drops decreases for larger ζ. The fluid temperature drops with the augmenting Pr values. The drop in $\theta(\zeta)$ is dominant for the intermediate ζ values. The reason for the temperature drop of the Carreau fluid with the ascending Pr is due to the decreasing values of the Carreau fluid thermal diffusivity. Figure 13b displays that the temperature enhances with higher radiation parameter Rd values. The increase in the $\theta(\zeta)$ profiles of the Carreau fluid with larger Rd is more obvious for the smaller values of ζ.

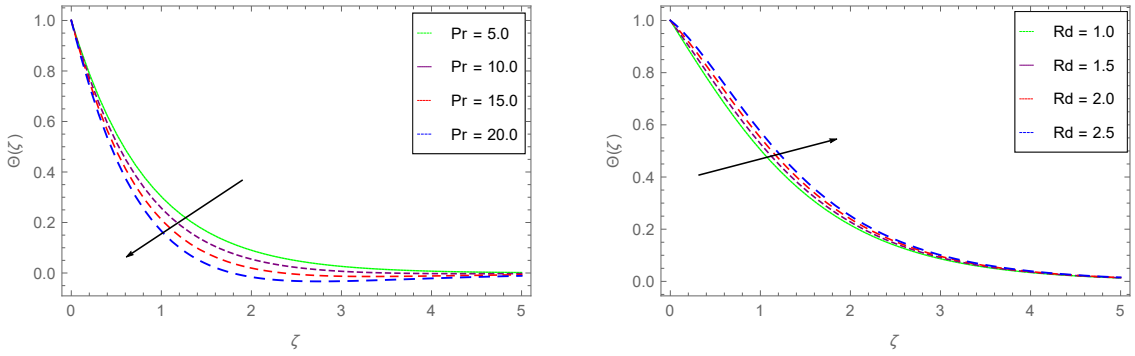

(**a**) (**b**)

Figure 13. (**a**) Impact of Pr on $\theta(\zeta)$ and (**b**) influence of Rd on $\theta(\zeta)$.

The impacts of the internal heat source parameter γ and stretching rate ratio c on the temperature distribution of the Carreau fluid are depicted in Figure 14a,b, respectively. It is obvious from Figure 14a that the fluid temperature drops as we go away from the wall (at larger ζ). Furthermore, the temperature rises with the rising γ values. The temperature of the fluid first rises, reaches maximum value, then drops with increasing ζ at constant stretching rate ratio (c). The augmenting values of the stretching rate ratio first drop the fluid temperature up to about $\zeta = 1.0$ and then enhance it beyond $\zeta = 1.0$.

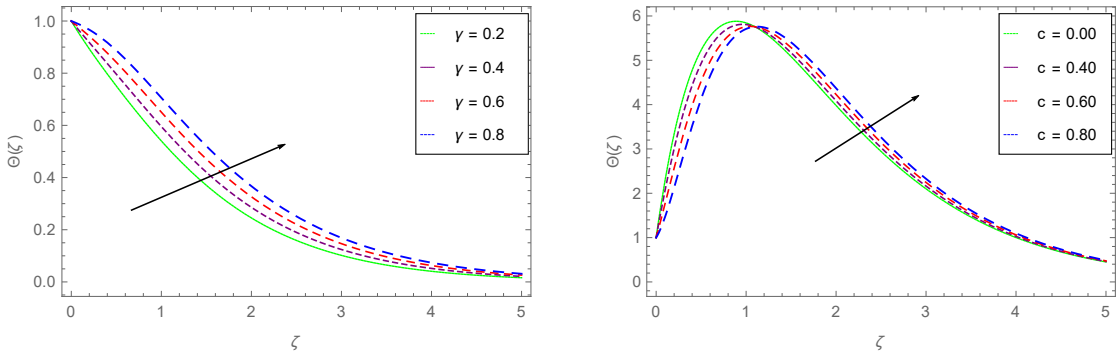

(**a**) (**b**)

Figure 14. Dependence of $\theta(\zeta)$ on (**a**) γ and (**b**) c.

The influence of the internal source reflection terms $\tilde{A}$ and $\tilde{B}$ on the Carreau fluid temperature $\theta(\zeta)$ are respectively displayed in Figure 15a,b. Both figures show that the increasing values of the reflection terms $\tilde{A}$ and $\tilde{B}$ cause an enhancement in the temperature. Both these terms have approximately the same influence over the enhancement in $\theta(\zeta)$. Thus, the positive values of the reflection terms augment the Carreau fluid temperature.

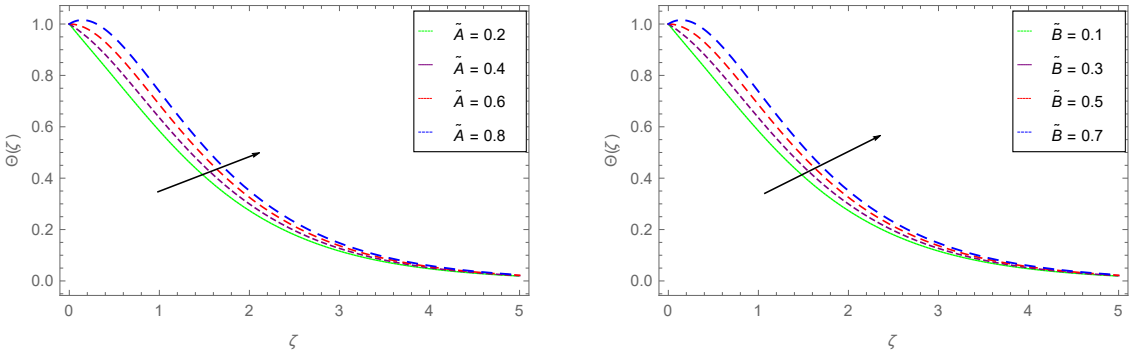

Figure 15. (**a**) Effect of $\tilde{A}$ on ($\theta(\zeta)$) and (**b**) influence of $\tilde{B}$ on $\theta(\zeta)$.

Figure 16a,b respectively show the impact of the variation of the thermoporesis and Brownian motion parameters over the Carreau fluid concentration $\Phi(\zeta)$. We observe that at a given value of Nt, the fluid concentration drops as ζ increases. The rising Nt values cause an enhancement of the fluid concentration. This increase in concentration is more dominant at the smaller values of ζ. The increase in fluid concentration due to higher Nt may be associated with the existence of larger concentration gradients. We also observe an increase in the fluid concentration with the ascending Nb values. The increase in the fluid concentration is more drastic for the highest Nb. This enhancement of fluid concentration may be due to the higher rate of random collisions between fluid particles.

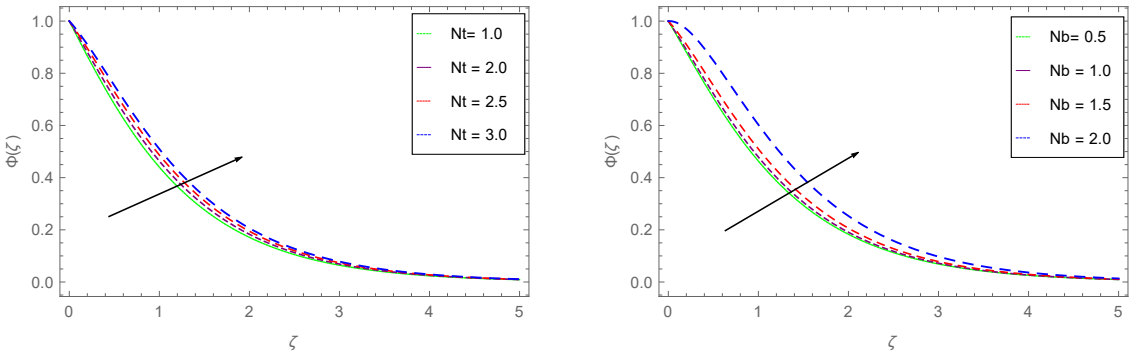

Figure 16. (**a**) $\Phi(\zeta)$ dependence on Nt. (**b**) $\Phi(\zeta)$ dependence on Nb.

The dependence of the Carreau fluid concentration $\Phi(\zeta)$ on the changing Schmidt number Sc is shown in Figure 17a, and $\hat{k}$ (chemical reaction rate parameter) is pictured in Figure 17b. We can see from Figure 17a that the ascending values of Sc raise the fluid concentration. The enhancement in $\Phi(\zeta)$ is more prominent for smaller ζ values. This physically means that the higher momentum diffusivity causes enhancement in the fluid concentration. Figure 17b displays that the rising $\hat{k}$ values drop the fluid concentration. The reduction in the fluid concentration is more dominant at small ζ values.

The dependence of Sherwood number on Schmidt number (Sc) and reaction rate parameter ($\hat{k}$) is respectively displayed in Figure 18a,b. We see from Figure 18a that at a given Sc, the Sherwood number drops with higher ζ. As the values of Sc are enhanced, the Sherwood number profiles drop. This drop in Sherwood number is more drastic at higher values of ζ. Figure 18b depicts that Sherwood number enhances with increasing values of thermal reaction rate parameter $\hat{k}$.

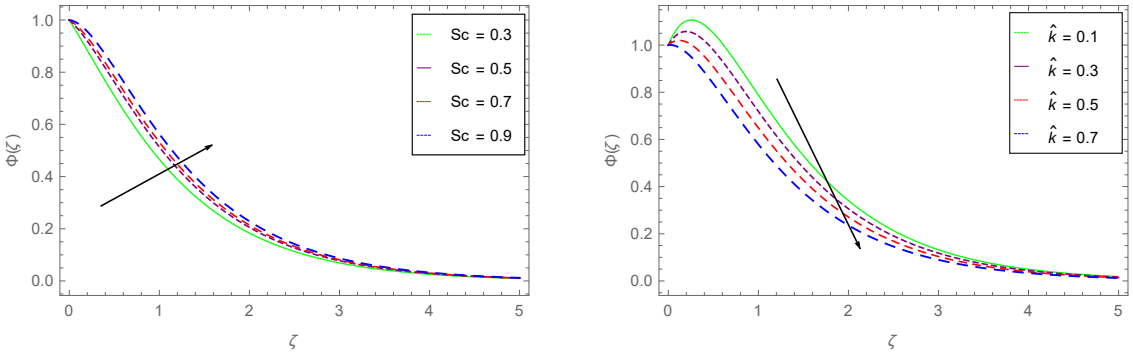

(**a**) (**b**)

Figure 17. Impact of (**a**) Sc on $\Phi(\zeta)$ and (**b**) $\hat{k}$ on $\Phi(\zeta)$.

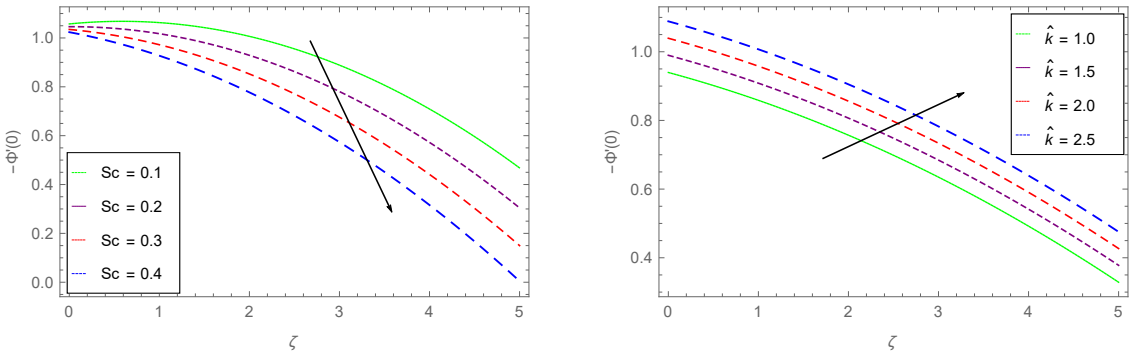

(**a**) (**b**)

Figure 18. Dependence of Sherwood number on (**a**) Sc and (**b**) $\hat{k}$.

The impact of increasing values of radiation and Brownian motion parameters (Rd and Nb) on Nusselt number is plotted respectively in Figure 19a,b. It is clear from Figure 19a that the Nusselet number varies inversely with higher values of ζ at a given value of Rd. The Nusselet number enhances with higher values of Rd almost at the same rate. Figure 19b shows that the Nusselt number enhances with rising Nb values. The spacing between different curves for varying Nb values decreases at the intermediate values of ζ.

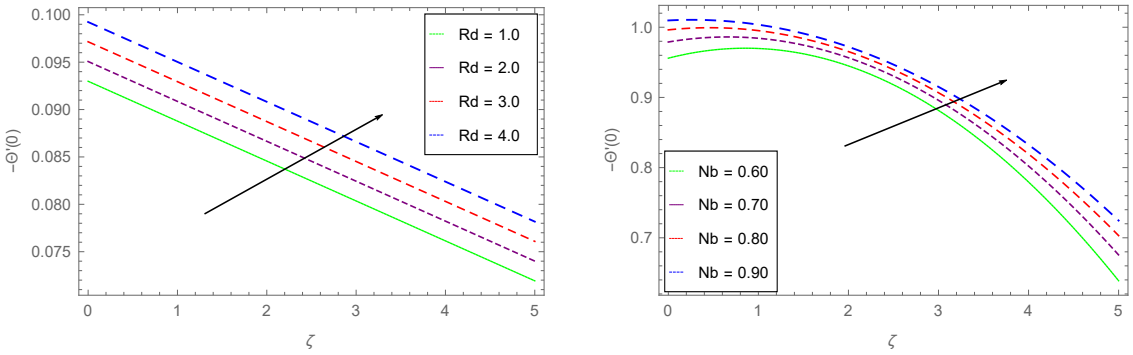

(**a**) (**b**)

Figure 19. Dependence of Nusselt number on (**a**) Rd and (**b**) Nb.

The impact of M (magnetic parameter) on the skin friction (C_{fx}) along x-axis is shown in Figure 20a. We observe that the C_{fx} augments with rising values of ζ at fixed M. By increasing the magnetic field

strength, C_{fx} enhances with an almost uniform amount. Figure 20b is the graphical representation of the skin friction C_{fy} along y-axis with varying values of stretching rate ratio c. We see that C_{fy} drops with the augmenting values of c almost at the same rate.

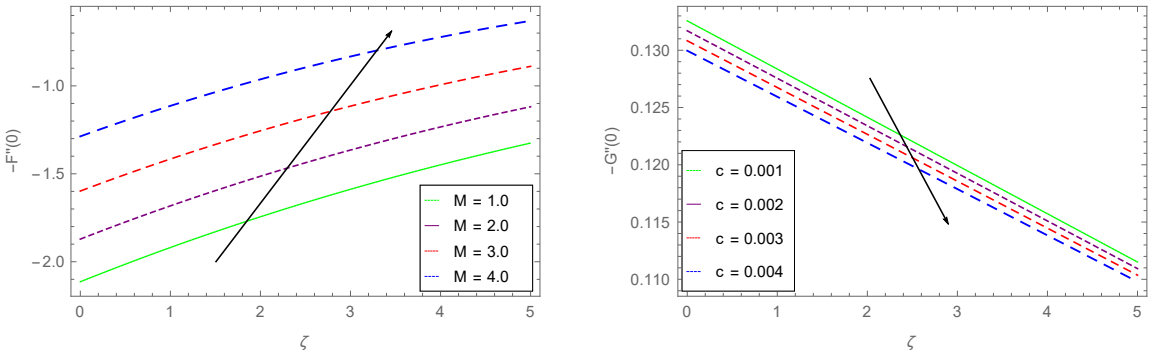

(**a**) (**b**)

Figure 20. (**a**) The dependence of skin friction (C_{fx}) on M. (**b**) The dependence of skin friction (C_{fy}) on c.

5. Tables Discussion

The engineering quantities of interest are explained in this section. Tables 1–3 show the impact of varying values of various parameters over the Nusselt number, skin frictions, and Sherwood number, respectively.

The comparison between the results achieved in this study and the already published results for the computation of Nusselt number for the nonzero Schmidt number and Brownian motion parameter is displayed in Table 1. We see an excellent agreement in both results.

Table 1. Impact of the variation of Pr on Nusselt number for the nonzero values of the Schmidth number and the Brownian motion parameter.

Pr	$-\Theta'(0)$	Present Results $-\Theta'(0)$
0.07	0.065663	0.06566331
0.09	0.075853	0.07585343
1.00	0.231285	0.23128545
2.00	0.911489	0.91148934
7.00	1.89547	1.8954745

The skin frictions along the x-axis (C_{fx}) and y-axis (C_{fx}) are computed for varying values of ζ, Λ, and We in Table 2.

Table 2. Different values of $-F''(0)$ and $-G''(0)$ for varying ς, Λ, and We.

ς	Λ	We	$-F''(0)$	$-G''(0)$
0.2	2.0	0.5	1.6712950	2.2421201
0.3			1.4316711	3.7195922
0.4			2.4720023	3.7195923
0.5			2.395264	2.8854775
0.2	2.8		2.2742042	2.6856884
	3.0		2.1943074	2.6725891
	3.5		1.6060401	2.2080583
	2.0	0.8	1.8030313	2.0519016
		0.9	1.8354931	2.5575852
		1.0	2.0481525	3.4036193

The Nusselt and Sherwood numbers are computed for various values of Nb, Rd, $\hat{k}$, and Pr in Table 3.

Table 3. Calculation of $-\Theta'(0)$ and $-\Phi'(0)$ for varying Nb, Rd, $\hat{k}$, and Pr by keeping the remaining parameters fixed.

Nb	Rd	$\hat{k}$	Pr	$-\Theta'(0)$	$-\Phi'(0)$
0.1	0.4	0.5	0.72	0.3017291	1.2785483
0.3				0.2454834	1.3708325
0.5				0.1994182	1.3939463
0.7				0.1605945	1.4063601
0.1	0.5			0.2877691	1.3219014
	0.6			0.2707055	1.3749094
	0.7			0.2488083	1.4428653
	0.4	0.4		0.3022361	1.2716452
		0.2		0.3032192	1.2583444
		0.1		0.30370646	1.251925
		0.5	0.78	0.3146993	1.2617091
			0.84	0.3278921	1.2434992
			0.90	0.3413793	1.2236714

6. Conclusions

We examined the impact of chemical reaction rate and Brownian motion parameters on the MHD Carreau fluid 3-dimensional flow by using thermal radiation and mass transfer analysis. A simplified set of coupled second order ODEs is obtained through suitable transformation relations. These coupled ODEs are solved by using the homotopy analysis method (HAM). The influence of magnetic filed, stretching rate ratio, Weissenberg number, Grashof number, chemical reaction rate and Brownian motion parameters, Schmidt number, and other parameters are explained through various graphs. The agreement of achieved and published results confirms the accuracy of the employed procedure. We concluded the following main points:

- The horizontal velocity components ($F^{'}(\zeta)$ and $G^{'}(\zeta)$) drop with the ascending M.
- The enhancement in the stretching rate ratio drops the shear stress horizontal and vertical velocity profiles ($G^{''}(\zeta)$, $F^{'}(\zeta)$, $F(\zeta)$) and enhances the ($F^{''}(\zeta)$, $G^{'}(\zeta)$, $G(\zeta)$) profiles.
- The horizontal and vertical velocity profiles (($F^{'}(\zeta)$, $G^{'}(\zeta)$, $F(\zeta)$, $G(\zeta)$) augment, while the shear stress profiles ($F^{''}(\zeta)$, $G^{''}(\zeta)$) drop with the ascending Grashof number values.
- The fluid temperature augments with the higher values of all pertinent parameters except Prandtl number.
- The fluid concentration augments with the higher values of thermoporesis and Brownian motion parameters, and Schmidt number, while drops with the higher values of the parameter of chemical reaction rate.
- The Nusselt number augments with the increasing radiation and Brownian motion parameters.
- The skin friction C_{fx} along x-axis augments with the augmenting magnetic parameter values, and along the y-axis C_{fy} drops with the rising stretching rate ratio.
- The agreement between obtained and published results confirms the accuracy of our employed analytical technique.

Author Contributions: Conceptualization, A.U. and I.; Software, W.K. and T.A.; Writing—Original Draft Preparation, W.K. and M.A.; Writing—Review and Editing, H.U.K, M.A., T.A. and I.; Formal Analysis, H.A, H.U.K. and M.A.; Validation, A.U. and W.K.; Methodology, A.U., W.K. and H.A.; Investigation, I., I.K. and A.U.; Resources, I.K. and H.A.; Project Administration, T.A. and H.A. All authors have read and agreed to the published version of the manuscript.

Funding: This research received no external funding.

Acknowledgments: The authors are thankful to anonymous reviewers for their fruitful suggestion which improved the quality of the manuscript.

Conflicts of Interest: The authors declare no conflict of interest.

Abbrevations

The below mentioned parameters and abbreviations with their possible dimensions are used in this article:

σ^*	Electrical conductivity $\frac{S}{m}$
B	Uniform magnetic parameter strength T
$Nu_{x,y}$	Nusslet number along x-axis and y-axis
Re_x	Local Reynolds number
C_{fx}	Skin friction along the x-axis
C_{fy}	Skin friction along the y-axis
Sh_x	Sherwood number
D_m	Mass diffusivity parameter
Pr	Prandtl number
u_w	Constant Fluid velocity $(\frac{m}{sec})$
T	Fluid temperature (K)
v	Kinematic viscosity $\frac{m^2}{sec}$
ρ	Density $(\frac{Kg}{m^3})$
μ	Dynamic viscosity mPa
C_p	Specific heat $(\frac{J}{KgK})$
Sc	Schmidt number
f, g	Dimensionless velocities
θ	Dimensionless temperature
ϕ	Dimensionless concentration
∞	Condition at infinity
0	Reference condition
x, y, and z	Coordinates (m)
η	Similarity variable
ψ	Stream function
Nb	Brownian motion parameter
Nt	Thermophoresis parameter
t	Time (sec)
n	Power law index
M	Magnetic field interaction parameter
τ	Extra stress tensor
σ^s	Stefan Boltzmann constant
F, G	Restricted dimensionless velocity components along x and y-axis respectively.
Θ	Restricted dimensionless temperature
Φ	Restricted dimensionless concentration
q_s	Surface heat transfer
$\hat{k}$	Chemical reaction parameter
Γ	Time constant
k_1	Average absorption coefficient
We	Weissenberg number
Gr	Grashof number
$\tilde{A}, \tilde{B}$	Internal heat generation parameters
γ	Internal heat source and sink

References

1. Carreau, P.J. Rheological equations from molecular network theories. *Trans. Soc. Rheol.* **1972**, *16*, 99–127. [CrossRef]
2. Carreau, P.; Kee, D.D.; Daroux, M. An analysis of the viscous behaviour of polymeric solutions. *Can. J. Chem. Eng.* **1979**, *57*, 135–140. [CrossRef]
3. Bush, M.; Phan-Thien, N. Drag force on a sphere in creeping motion throug a carreau model fluid. *J. Non-Newton. Fluid Mech.* **1984**, *16*, 303–313. [CrossRef]
4. Khellaf, K.; Lauriat, G. Numerical study of heat transfer in a non-Newtonian Carreau-fluid between rotating concentric vertical cylinders. *J. Non-Newton. Fluid Mech.* **2000**, *89*, 45–61. [CrossRef]
5. Khan, M.; Sardar, H.; Gulzar, M.M.; Alshomrani, A.S. On multiple solutions of non-Newtonian Carreau fluid flow over an inclined shrinking sheet. *Results Phys.* **2018**, *8*, 926–932. [CrossRef]
6. Olajuwon, I.B. Convection heat and mass transfer in a hydromagnetic Carreau fluid past a vertical porous plate in presence of thermal radiation and thermal diffusion. *Thermal Sci.* **2011**, *15*, 241–252. [CrossRef]
7. Hsu, J.P.; Shie, C.F.; Tseng, S. Sedimentation of a cylindrical particle in a Carreau fluid. *J. Colloid Interface Sci.* **2005**, *286*, 392–399. [CrossRef]
8. Ali, N.; Hayat, T. Peristaltic motion of a Carreau fluid in an asymmetric channel. *Appl. Math. Comput.* **2007**, *193*, 535–552. [CrossRef]
9. Hayat, T.; Saleem, N.; Ali, N. Effect of induced magnetic field on peristaltic transport of a Carreau fluid. *Commun. Nonlinear Sci. Numer. Simul.* **2010**, *15*, 2407–2423. [CrossRef]
10. Tshehla, M. The flow of Carreau fluid down an incline with a free surface. *Int. J. Phys. Sci* **2011**, *6*, 3896–3910.
11. Ellahi, R.; Riaz, A.; Nadeem, S.; Ali, M. Peristaltic flow of Carreau fluid in a rectangular duct through a porous medium. *Math. Probl. Eng.* **2012**, *2012*. [CrossRef]
12. Ishak, A.; Nazar, R.; Pop, I. Hydromagnetic flow and heat transfer adjacent to a stretching vertical sheet. *Heat Mass Transf.* **2008**, *44*, 921. [CrossRef]
13. Ishak, A.; Jafar, K.; Nazar, R.; Pop, I. MHD stagnation point flow towards a stretching sheet. *Physica A* **2009**, *388*, 3377–3383. [CrossRef]
14. Xu, H.; Liao, S.J.; Pop, I. Series solutions of unsteady three-dimensional MHD flow and heat transfer in the boundary layer over an impulsively stretching plate. *Eur. J. Mech.-B/Fluids* **2007**, *26*, 15–27. [CrossRef]
15. Vajravelu, K.; Hadjinicolaou, A. Convective heat transfer in an electrically conducting fluid at a stretching surface with uniform free stream. *Int. J. Eng. Sci.* **1997**, *35*, 1237–1244. [CrossRef]
16. Pop, I.; Na, T.Y. A note on MHD flow over a stretching permeable surface. *Mech. Res. Commun.* **1998**, *25*, 263–269. [CrossRef]
17. Machireddy, G.R.; Polarapu, P.; Bandari, S. Effects of magnetic field and Ohmic heating on viscous flow of a nanofluid towards a nonlinear permeable stretching sheet. *J. Nanofluids* **2016**, *5*, 459–470. [CrossRef]
18. Liu, I.C.; Wang, H.H.; Peng, Y.F. Flow and heat transfer for three-dimensional flow over an exponentially stretching surface. *Chem. Eng. Commun.* **2013**, *200*, 253–268. [CrossRef]
19. Hayat, T.; Asad, S.; Mustafa, M.; Alsaedi, A. Boundary layer flow of Carreau fluid over a convectively heated stretching sheet. *Appl. Math. Comput.* **2014**, *246*, 12–22. [CrossRef]
20. Reddy, M.G. Influence of magnetohydrodynamic and thermal radiation boundary layer flow of a nanofluid past a stretching sheet. *J. Sci. Res.* **2014**, *6*, 257–272. [CrossRef]
21. AboEldahab, E.M. Radiation effect on heat transfer in an electrically conducting fluid at a stretching surface with a uniform free stream. *J. Phys. D Appl. Phys.* **2000**, *33*, 3180. [CrossRef]
22. Gnaneswara Reddy, M. Thermal radiation and chemical reaction effects on MHD mixed convective boundary layer slip flow in a porous medium with heat source and Ohmic heating. *EPJP* **2014**, *129*, 41. [CrossRef]
23. Abo-Eldahab, E.M.; El Gendy, M.S. Radiation effect on convective heat transfer in an electrically conducting fluid at a stretching surface with variable viscosity and uniform free stream. *Phys. Scr.* **2000**, *62*, 321. [CrossRef]
24. Reddy, M.G. Effects of Thermophoresis, Viscous Dissipation and Joule Heating on Steady MHD Flow over an Inclined Radiative Isothermal Permeable Surface with Variable Thermal Conductivity. *J. Appl. Fluid Mech.* **2014**, *7*, 51–61.

25. KRISNA, P.M.; SANDEEP, N.; SUGUNAMMA, V. Effects of radiation and chemical reaction on MHD convective flow over a permeable stretching surface with suction and heat generation. *Walailak J. Sci. Technol. (WJST)* **2015**, *12*, 831–847.
26. Sandeep, N.; Sulochana, C.; Sugunamma, V. Radiation and magnetic field effects on unsteady mixed convection flow over a vertical stretching/shrinking surface with suction/injection. *Ind. Eng. Lett.* **2015**, *5*, 127–136.
27. Jonnadula, M.; Polarapu, P.; Reddy, G. Influence of thermal radiation and chemical reaction on MHD flow, heat and mass transfer over a stretching surface. *Procedia Eng.* **2015**, *127*, 1315–1322. [CrossRef]
28. Das, S.; Jana, R.; Makinde, O. Magnetohydrodynamic mixed convective slip flow over an inclined porous plate with viscous dissipation and Joule heating. *Alexandria Eng. J.* **2015**, *54*, 251–261. [CrossRef]
29. Singh, G.; Makinde, O.D. Mixed convection slip flow with temperature jump along a moving plate in presence of free stream. *Thermal Sci.* **2015**, *19*, 119–128. [CrossRef]
30. Makinde, O.; Khan, W.; Culham, J. MHD variable viscosity reacting flow over a convectively heated plate in a porous medium with thermophoresis and radiative heat transfer. *Int. J. Heat Mass Transf.* **2016**, *93*, 595–604. [CrossRef]
31. Ibrahim, W.; Makinde, O. Magnetohydrodynamic stagnation point flow and heat transfer of Casson nanofluid past a stretching sheet with slip and convective boundary condition. *J. Aerosp. Eng.* **2016**, *29*, 04015037. [CrossRef]
32. Hayat, T.; Muhammad, T.; Shehzad, S.A.; Alsaedi, A. Simultaneous effects of magnetic field and convective condition in three-dimensional flow of couple stress nanofluid with heat generation/absorption. *J. Braz. Soc. Mech. Sci. Eng.* **2017**, *39*, 1165–1176. [CrossRef]
33. Abbasi, F.; Shehzad, S.; Hayat, T.; Ahmad, B. Doubly stratified mixed convection flow of Maxwell nanofluid with heat generation/absorption. *J. Magn. Magn. Mater.* **2016**, *404*, 159–165. [CrossRef]
34. Shehzad, S.; Abdullah, Z.; Alsaedi, A.; Abbasi, F.; Hayat, T. Thermally radiative three-dimensional flow of Jeffrey nanofluid with internal heat generation and magnetic field. *J. Magn. Magn. Mater.* **2016**, *397*, 108–114. [CrossRef]
35. Hayat, T.; Muhammad, T.; Shehzad, S.A.; Alsaedi, A.; Al-Solamy, F. Radiative three-dimensional flow with chemical reaction. *Int. J. Chem. React. Eng.* **2016**, *14*, 79–91. [CrossRef]
36. Shehzad, S.; Hayat, T.; Alsaedi, A. Three-dimensional MHD flow of Casson fluid in porous medium with heat generation. *J. Appl. Fluid Mech.* **2016**, *9*, 215–223. [CrossRef]
37. Machireddy, G.R. Chemically reactive species and radiation effects on MHD convective flow past a moving vertical cylinder. *Ain Shams Eng. J.* **2013**, *4*, 879–888. [CrossRef]
38. Raju, C.; Ibrahim, S.; Anuradha, S.; Priyadharshini, P. Bio-convection on the nonlinear radiative flow of a Carreau fluid over a moving wedge with suction or injection. *Eur. Phys. J. Plus* **2016**, *131*, 1–16. [CrossRef]
39. Raju, C.; Sandeep, N. Opposing and assisting flow characteristics of radiative Casson fluid due to cone in the presence of induced magnetic field. *Int. J. Adv. Sci. Technol.* **2016**, *88*, 43–62. [CrossRef]
40. Akbar, N.S.; Nadeem, S. Carreau fluid model for blood flow through a tapered artery with a stenosis. *Ain Shams Eng. J.* **2014**, *5*, 1307–1316. [CrossRef]
41. Suneetha, S.; Gangadhar, K. Thermal radiation effect on MHD stagnation point flow of a Carreau fluid with convective boundary condition. *Open Sci. J. Math. Appl.* **2015**, *3*, 121.
42. Durga Prasad, P.; Varma, S.; Raju, C.; Shehzad, S.A.; Meraj, M. 3D flow of Carreau polymer fluid over variable thickness sheet in a suspension of microorganisms with Cattaneo-Christov heat flux. *Revista Mexicana de Física* **2018**, *64*, 519–529. [CrossRef]
43. Ibrahim, W.; Gizewu, T. Nonlinear mixed convection flow of a tangent hyperbolic fluid with activation energy. *Heat Transf.* **2020**. [CrossRef]
44. Kumaran, G.; Sandeep, N. Thermophoresis and Brownian moment effects on parabolic flow of MHD Casson and Williamson fluids with cross diffusion. *J. Mol. Liq.* **2017**, *233*, 262–269. [CrossRef]
45. Abegunrin, O.; Okhuevbie, S.; Animasaun, I. Comparison between the flow of two non-Newtonian fluids over an upper horizontal surface of paraboloid of revolution: Boundary layer analysis. *Alex. Eng. J.* **2016**, *55*, 1915–1929. [CrossRef]
46. Liao, S.J. The Proposed Homotopy Analysis Technique for the Solution of Nonlinear Problems. Ph.D. Thesis, Shanghai Jiao Tong University Shanghai, Shanghai, China, 1992.

47. Sajid, M.; Hayat, T. Comparison of HAM and HPM methods in nonlinear heat conduction and convection equations. *Nonlinear Anal. Real World Appl.* **2008**, *9*, 2296–2301. [CrossRef]
48. Zhu, J.; Zheng, L.; Zheng, L.; Zhang, X. Second-order slip MHD flow and heat transfer of nanofluids with thermal radiation and chemical reaction. *Appl. Math. Mech.* **2015**, *36*, 1131–1146. [CrossRef]